

**IMPERIAL**

## **Final Report for MEng Bioengineering Individual Project**

---

### **Modelling LSD Effects on Neurovascular Parameters in Resting-State fMRI: A Comparison of Physiological and Spectral Dynamic Causal Approaches**

---

*Author:*

*Bay Chin (CID: 02015483)*

*Supervisor(s):*

*Dr. Marta Varela*

*Dr. Pedro Mediano*

*Submitted in partial fulfilment of the requirements for the award of MEng in Biomedical Engineering from Imperial College London*

*Date: June 10, 2025*

*Word Count: 5947*

# Contents

<b>Acknowledgements</b>	<b>3</b>
<b>1 Introduction</b>	<b>4</b>
<b>2 Contributions</b>	<b>5</b>
<b>3 Background</b>	<b>5</b>
3.1 Functional Magnetic Resonance Imaging (fMRI) . . . . .	5
3.2 Psychedelic Reorganisation of Brain Networks and Implications for fMRI . . . . .	6
3.3 Dynamic Causal Modelling (DCM) . . . . .	6
3.3.1 Physiologically Informed Dynamic Causal Modelling (P-DCM) . . . . .	6
3.3.2 Bridging Time and Frequency Domains: The Transfer Function . . . . .	8
3.3.3 Spectral Dynamic Causal Modelling (spDCM) . . . . .	8
3.4 Optimisation Techniques in DCM . . . . .	9
<b>4 Methods</b>	<b>9</b>
4.1 Data Acquisition and Ethics . . . . .	9
4.2 Implementation of P-DCM Model . . . . .	9
4.3 Implementation of spDCM Model . . . . .	10
4.4 Implementation of the Optimisation Framework . . . . .	10
<b>5 Results</b>	<b>11</b>
5.1 Empirical vs Model-Predicted PSDs (PLCB Condition) . . . . .	11
5.2 Model Comparisons: Efficiency and Fit Accuracy . . . . .	12
5.3 Performance Improvement Over Literature-Based Baselines . . . . .	12
5.4 Parameter Correspondence Between P-DCM and spDCM . . . . .	13
5.5 Empirical vs Model-Predicted PSDs (LSD Condition) . . . . .	13
5.6 Cortical Surface Mapping of LSD-Induced Parameter Changes . . . . .	14
5.7 Network-Level Statistical Mapping of Parameter Changes . . . . .	15
5.8 Univariate Cluster-Based Permutation Testing (Per-Parameter Across ROIs) . . . . .	17
5.9 Multi-Dimensional Cluster-Based Permutation Testing (Parameter × ROI) . . . . .	18
<b>6 Discussion</b>	<b>19</b>
6.1 Limitations and Constraints . . . . .	20
6.2 Future Work . . . . .	20
<b>7 Conclusion</b>	<b>21</b>
<b>A Appendix</b>	<b>24</b>
A.1 Literature Values from Havlicek et al. and Novelli et al. . . . .	24
A.2 ROI Indices and Corresponding Functional Network . . . . .	25
A.3 P-DCM vs spDCM Correlation . . . . .	26
A.4 Cortical Surface Projections of LSD vs. PLCB Parameter Differences (Paired <i>t</i> -tests) . . . . .	27
A.5 Network-Level Statistical Maps for Parameter Estimates . . . . .	28

## Acknowledgements

I would like to express my sincere gratitude to my supervisor, Dr. Marta Varela Anjari, and co-supervisor, Dr. Pedro Mediano, for their guidance, patience, insightful feedback, and invaluable support throughout this project.

I am also deeply grateful to my family—my parents, for their hard work and sacrifices in providing me with the best opportunities, and my sister, whose unwavering support, even from across the world, has been a cornerstone of my journey. I would not be where I am today without them.

Finally, I would like to thank my friends—from those who have been with me since the beginning to those I have grown closer to towards the end of the course—for their constant encouragement. Their belief in me is more than words can express, and they have made my time at Imperial College London unforgettable.

# Modelling LSD Effects on Neurovascular Parameters in Resting-State fMRI: A Comparison of Physiological and Spectral Dynamic Causal Approaches

Bay Chin

Department of Bioengineering, Imperial College London, United Kingdom

## Abstract

Dynamic causal modelling (DCM) provides a biophysical framework for inferring neural and vascular processes from resting-state functional MRI (rs-fMRI). This study compares two DCM variants—Physiological DCM (P-DCM), which models neurovascular coupling using stochastic differential equations in the time domain, and Spectral DCM (spDCM), which estimates effective connectivity from cross-spectral densities in the frequency domain—under placebo and lysergic acid diethylamide (LSD) conditions. Analyses focused on power spectral densities of individual brain regions to characterise local signal dynamics. Both models were applied to rs-fMRI data parcellated into 100 cortical regions. P-DCM more accurately captured the spectral complexity of empirical BOLD signals, yielding significantly lower normalised mean squared error than spDCM. While P-DCM required greater computational resources, it produced more stable parameter estimates across subjects and conditions. These advantages persisted under LSD, a condition known to alter neuronal and vascular function, whereas spDCM showed reduced fit quality and greater variability. Despite modelling the same data, parameter estimates from the two models were uncorrelated, reflecting differences in computational architecture. Although paired *t*-tests did not yield significant results after correction for multiple comparisons, two cluster-based permutation tests—univariate and multidimensional—identified significant LSD-related changes in P-DCM parameters. These included spatially coherent alterations in neurovascular gain, mean transit time, spectral slope of endogenous fluctuations, and excitatory self-inhibition, primarily in visual, salience, and default mode networks. One significant cluster was also observed in spDCM for phase-based connectivity within the default mode network. These findings highlight the impact of modelling approach on sensitivity to physiological changes in resting-state brain dynamics.

## 1.0 Introduction

Non-invasive neuroimaging techniques, particularly functional magnetic resonance imaging (fMRI), have significantly advanced our understanding of the brain's functional architecture. The blood-oxygen-level-dependent (BOLD) signal derived from fMRI reflects neurovascular coupling (NVC)—the process through which neural activity modulates local cerebral blood flow and oxygenation [1]. Resting-state fMRI (rs-fMRI), which measures spontaneous low-frequency fluctuations in the BOLD signal, is commonly used to investigate the brain's intrinsic functional organisation without task-related influences [2]. Accurate characterisation of NVC dynamics is essential for interpreting fMRI data and understanding

how neural and vascular systems interact, particularly in contexts involving altered brain states.

One such context is the administration of psychedelic compounds, which are gaining attention in both basic neuroscience and clinical psychiatry. Psychedelics such as lysergic acid diethylamide (LSD) are known to induce profound changes in awareness and have shown promise in the treatment of conditions including depression, anxiety, and post-traumatic stress disorder (PTSD) [3]. Investigating how these substances influence brain dynamics not only deepens our understanding of conscious experience but also informs potential therapeutic mechanisms. Recent studies suggest that psychedelics influence both NVC and effective connectivity—defined as

the directed influence one brain region exerts over another—resulting in distinct changes in the BOLD signal [4][5].

Dynamic causal modelling (DCM) offers a principled framework for estimating directed brain connectivity and biophysical parameters underlying the BOLD response. Among the various DCM approaches, two are pertinent to this study: Physiological DCM (P-DCM), which models NVC through differential equations grounded in biophysical processes [6], and Spectral DCM (spDCM), which operates in the frequency domain. While P-DCM provides a detailed representation of haemodynamic mechanisms, spDCM offers computational efficiency suitable for large-scale inference [7]. However, both approaches have limitations when applied to brain states perturbed by psychedelic compounds, motivating a comparative investigation of their suitability for modelling psychedelic-induced brain states.

Accordingly, this study aims to model LSD-induced changes in neurovascular parameters in rs-fMRI by evaluating and comparing the capacity of P-DCM and spDCM to model neurovascular changes induced by LSD.

## 2.0 Contributions

The primary contributions of this study are as follows:

- Implementation of P-DCM and spDCM Frameworks:** Developed and applied both P-DCM and spDCM frameworks to model rs-fMRI data under placebo (PLCB) and LSD conditions.
- Parameter Estimation and Model Evaluation:** Leveraged machine learning optimisation to estimate neuronal, neurovascular, and haemodynamic parameters, with model performance assessed by accuracy, runtime, and comparison to literature-based benchmarks.
- Analysis of LSD-Induced Physiological Changes:** Conducted paired *t*-tests on parameter estimates across conditions, with statistical and spatial characterisation at both ROI and network levels, including effect size

analysis and permutation-based cluster testing.

- Framework for Future Neurovascular Modelling:** Identified trade-offs between model accuracy and efficiency, and proposed extensions using Physics-Informed Neural Networks (PINNs) and Deep Operator Networks (DeepONets) for scalable, interpretable neurovascular modelling in altered states of consciousness. [8][9].

## 3.0 Background

### 3.1 Functional Magnetic Resonance Imaging (fMRI)

fMRI is a non-invasive neuroimaging technique that maps brain activity by detecting changes in blood oxygenation levels [10]. The BOLD signal arises from a delayed, non-linear vascular response to underlying neural activity, mediated by changes in cerebral blood flow (CBF), cerebral blood volume (CBV), and the cerebral metabolic rate of oxygen consumption (CMRO<sub>2</sub>) [11].

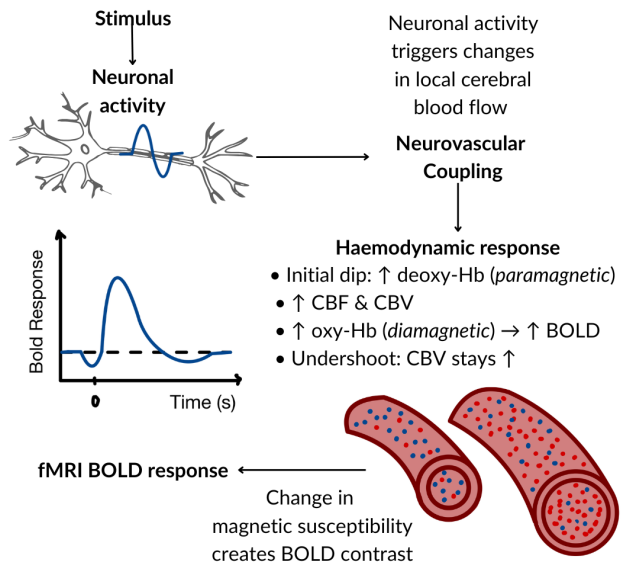


**Figure 1.** Schematic of the biophysical processes linking neuronal activity to the fMRI BOLD signal via NVC and haemodynamic changes.

Neuronal activation increases local metabolic demand, transiently elevating deoxygenated haemoglobin (deoxyHb) levels due to increased oxygen extraction. In response, vasodilation induces a compensatory rise in CBF, leading to an

oversupply of oxygenated haemoglobin (oxyHb) and a net reduction in deoxyHb concentration. This shift alters the magnetic susceptibility of surrounding tissue: oxyHb, being diamagnetic, has minimal effect on the local magnetic field, whereas paramagnetic deoxyHb introduces field inhomogeneities that accelerate T2\* relaxation, thereby reducing BOLD signal intensity [12].

The BOLD signal thus reflects a spatially and temporally filtered transformation of neuronal activity, governed by NVC [13]. Acting as a low-pass filter, NVC introduces delays and suppresses rapid neural fluctuations. Consequently, BOLD fMRI offers an indirect, smoothed representation of neural activity shaped by vascular dynamics. Moreover, individual differences in vascular physiology can affect signal interpretation—particularly when haemodynamic models assume uniform response properties across subjects or brain regions [14].

These limitations motivate biophysically grounded modelling approaches that aim to disentangle vascular and neuronal contributions to the BOLD signal. This need is particularly salient in non-ordinary states of consciousness, where neuromodulatory compounds such as LSD may influence both neural activity and vascular dynamics. Accordingly, this study employs biophysically informed DCMs to investigate how LSD affects neurovascular parameters in rs-fMRI.

### 3.2 Psychedelic Reorganisation of Brain Networks and Implications for fMRI

Psychedelics such as LSD are of growing interest for their capacity to disrupt maladaptive neural patterns and promote large-scale reorganisation of brain network dynamics [3][15][16]. fMRI studies report increased neural signal entropy and more distributed, less modular functional connectivity under psychedelics, reflecting greater neural flexibility and shifts in conscious state [17][18][19].

These effects complicate the interpretation of BOLD fMRI signals, as traditional analyses often assume stable NVC and may misattribute vascular contributions to neural activity [20].

LSD, in particular, acts primarily via 5-HT2A receptor agonism, influencing glutamate signalling and reducing default mode network (DMN) activity [21][22]. Such widespread physiological changes may disrupt canonical haemodynamic responses and challenge the assumptions of fixed-form models.

Understanding how psychedelics reorganise large-scale brain networks and influence neurovascular dynamics is essential for accurately interpreting BOLD signals under altered brain states. This also motivates the use of biomarkers to enhance diagnostic precision and treatment monitoring in psychiatric conditions characterised by disrupted connectivity or atypical neurovascular responses.

### 3.3 Dynamic Causal Modelling (DCM)

DCM is a Bayesian framework that estimates directed (causal) interactions among neuronal populations by modelling the neuronal and haemodynamic processes underlying fMRI data [23].

#### 3.3.1 Physiologically Informed Dynamic Causal Modelling (P-DCM)

P-DCM describes NVC using a system of non-linear differential equations that link neuronal activity to the BOLD response [6]. It integrates excitatory–inhibitory dynamics, vascular signalling, and haemodynamic responses within a unified framework.

#### Neuronal Dynamics: Adaptive Two-State Model

P-DCM incorporates a two-state neuronal model consisting of excitatory  $x_E(t)$  and inhibitory  $x_I(t)$  populations, whose interactions evolve according to:

$$\frac{dx_E(t)}{dt} = -\sigma x_E(t) - \mu x_I(t) + cu(t) \quad (1)$$

$$\frac{dx_I(t)}{dt} = \lambda (x_E(t) - x_I(t)) \quad (2)$$

$u(t)$  is an exogenous input (e.g., a stimulus), and  $c$  is a coupling parameter that scales its influence on excitatory neuronal activity. The parameter  $\sigma$

represents excitatory self-decay and must be negative to ensure stability. The strength of inhibition onto excitatory neurons is scaled by  $\mu$ , while  $\lambda$  governs how inhibitory activity responds to excitatory input.

### Feedforward Neurovascular Coupling

Neuronal activity triggers changes in CBF, modelled via a vasoactive signal  $a(t)$ , which influences blood flow response  $f(t)$ :

$$\frac{da(t)}{dt} = -\varphi a(t) + x_E(t) \quad (3)$$

$$\frac{df(t)}{dt} = \phi a(t) - \chi(f(t) - 1) \quad (4)$$

These equations define a dynamic system in which the vasoactive signal acts as a low-pass filter on the neuronal input. The constant  $\phi$  and  $\varphi$  determines the gain and decay of the vasoactive signal respectively, and  $\chi$  controls the decay of blood inflow signal.

### Haemodynamic Response: Balloon Model with Viscoelasticity

The blood volume  $v(t)$  and deoxyHb content  $q(t)$  evolve according to the extended balloon model [24]:

$$\frac{dv(t)}{dt} = \frac{1}{\tau}(f(t) - f_{out}(v, t)) \quad (5)$$

$$\frac{dq(t)}{dt} = \frac{1}{\tau} \left( f(t) \frac{E(f)}{E_0} - f_{out}(v, t) \frac{q(t)}{v(t)} \right) \quad (6)$$

$$f_{out}(v, t) = \frac{1}{\tau_1 + \tau} (\tau + v(t)^{\frac{1}{\alpha}} + \tau_1 f(t)) \quad (7)$$

where  $\alpha$  is the Grubb's exponent,  $\tau$  is the mean transit time,  $\tau_1$  is the viscoelastic time,  $E(f) = 1 - (1 - E_0)^{1/f}$  models oxygen extraction, and  $f_{out}(v, t)$  is the blood outflow [6].

### BOLD Signal Generation

The resulting BOLD signal  $y(t)$  is modelled as:

$$y(t) = V_0 \left[ k_1 (1 - q(t)) + k_2 \left( 1 - \frac{q(t)}{v(t)} \right) + k_3 (1 - v(t)) \right] \quad (8)$$

$$k_1 = 4.3 \cdot v_0 \cdot E_0 \cdot TE \quad (9)$$

$$k_2 = \epsilon \cdot r_0 \cdot E_0 \cdot TE \quad (10)$$

$$k_3 = 1 - \epsilon \quad (11)$$

$V_0$  represents the resting blood volume fraction and acts as a scaling factor in the BOLD signal. Although  $V_0$  varies across regions, its exact value is typically not critical in DCM, as its influence can be counterbalanced by the scaling constant of neuronal activity. The parameters  $k_1$ ,  $k_2$ , and  $k_3$  are dimensionless constants reflecting tissue physiology and acquisition settings specific to the gradient echo (GE) sequence, and they depend on magnetic field strength.  $\epsilon$  represents the ratio of intra- to extra-vascular signal contributions.

### Network-Level Effective Connectivity

In multi-region DCMs, effective connectivity is represented by matrices that govern directed interactions among excitatory ( $X_E$ ) and inhibitory ( $X_I$ ) neural populations across cortical regions:

$$\frac{dX_E(t)}{dt} = \mathcal{J}X_E(t) + \mathcal{J}^-X_I(t) + Cu_d(t), \quad (12)$$

$$\frac{dX_I(t)}{dt} = \mathcal{G}(X_E(t) - X_I(t)), \quad (13)$$

Here,  $\mathcal{J}$  captures excitatory-to-excitatory coupling, while  $\mathcal{J}^-$  and  $\mathcal{G}$  reflect inhibitory feedback and inhibitory gain. The matrix  $C$  encodes how external inputs  $u_d(t)$  influence excitatory populations.

Each connectivity term is decomposed into fixed and modulatory components:

$$\mathcal{J}_{ij} = A_{ij} + \sum_{m=1}^M B_{ij}^{(m)} u_m(t), \quad (14)$$

$$\mathcal{J}_{ij}^- = \begin{cases} -\mu \exp \left( \tilde{\mu}_i + \sum_{k=1}^K b_{\mu i}^{(k)} u_{\mu k}(t) \right), & \text{if } i = j \\ 0, & \text{otherwise} \end{cases}, \quad (15)$$

$$\mathcal{G}_{ij} = \begin{cases} \lambda \exp \left( \tilde{\lambda}_i + \sum_{\ell=1}^L b_{\lambda i}^{(\ell)} u_{\lambda \ell}(t) \right), & \text{if } i = j \\ 0, & \text{otherwise} \end{cases}, \quad (16)$$

$$\mathcal{J}_{ii} = -\sigma \exp \left( \tilde{\sigma}_i + \sum_{n=1}^N b_{\sigma i}^{(n)} u_{\sigma n}(t) \right). \quad (17)$$

Here,  $A_{ij}$  represents baseline inter-regional coupling, and  $B_{ij}^{(m)}$  captures condition-specific modulation. Local connections ( $\mathcal{J}_{ii}, \mathcal{J}_{ii}^-, \mathcal{G}_{ii}$ ) use exponential parameterisations to enforce sign constraints (e.g., negativity for self-inhibition, positivity for gain) and enable condition-dependent scaling. Off-diagonal elements in  $\mathcal{J}^-$  and  $\mathcal{G}$  are zero, restricting these effects to within-region inhibitory control. This framework enables flexible and interpretable modelling of context-specific excitation–inhibition balance across the cortical hierarchy.

### 3.3.2 Bridging Time and Frequency Domains: The Transfer Function

While P-DCM models NVC via nonlinear differential equations in the time domain, spDCM operates in the frequency domain using CSDs. This frequency-domain formulation relies on a transfer function derived from the linearisation of the nonlinear haemodynamic system, allowing frequency-domain analysis via transfer function theory [25].

$$\begin{aligned} N(s) &= V_0 \phi [(E_0 - 1) \log(1 - E_0)(k_1 + k_2) \cdot \\ &\quad (\alpha s(\tau + \tau_1) + 1) - \alpha E_0(k_1 + k_3)(s\tau_1 + 1)] \\ D(s) &= E_0(s + \phi)(s + \chi)(s\tau_1 + 1)(\alpha s(\tau + \tau_1) + 1) \\ H(s) &= \frac{N(s)}{D(s)} \end{aligned} \quad (18)$$

where  $s = j\omega$ . The transfer function  $H(s)$  describes how endogenous neuronal fluctuations are transformed into BOLD signal fluctuations, accounting for both amplitude attenuation and phase shifts introduced by vascular dynamics.

### 3.3.3 Spectral Dynamic Causal Modelling (spDCM)

spDCM estimates effective connectivity by fitting observed CSDs to those predicted by a neuronal model convolved with a hemodynamic transfer function. This approach is especially useful for studying spontaneous brain activity in rs-fMRI because it uncovers mechanisms underlying cognition, sensory integration, and brain network dynamics across frequency bands.

spDCM uses power spectral densities (PSDs) to characterise activity within regions and CSDs to assess inter-regional interactions, bridging raw fMRI signals with neuronal interpretations. These spectral measures allow spDCM to characterise endogenous neural noise and isolate hemodynamic effects, improving interpretability of resting-state dynamics.

## Modelling Stochastic Neuronal Activity and Observation Noise

A key strength of spDCM lies in its capacity to model stochastic neuronal activity, which is critical for rs-fMRI data, where activity is driven by spontaneous neuronal fluctuations rather than external stimuli. Both state and observation noise are modelled as PSDs following a power-law decay, characterised by scaling factors ( $\alpha$ ) and decay exponents ( $\beta$ ) that describe how power decreases with frequency [7].

State noise,  $G_v(\omega)$ , reflects the frequency content of endogenous neuronal fluctuations:

$$G_v(\omega) = \alpha_v \omega^{-\beta_v} \quad (19)$$

Observation noise,  $G_e(\omega)$ , accounts for non-neuronal contributions to the measured BOLD signal:

$$G_e(\omega) = \alpha_e \omega^{-\beta_e} \quad (20)$$

## Mathematical Foundations of spDCM

spDCM operates within a Linear Time-Invariant (LTI) framework, in which input-output relationships are defined by linear systems with time-invariant parameters. This formalism enables the use of a haemodynamic transfer function  $H(\omega)$ , which characterises how neuronal activity is transformed into the observable BOLD signal across frequencies [7].

The neuronal frequency-domain response  $X(\omega)$  to endogenous inputs is given by:

$$X(\omega) = (i\omega I - A)^{-1}V(\omega) \quad (21)$$

where  $A$  is the effective connectivity matrix, and  $V(\omega)$  represents endogenous neuronal fluctuations.

The spDCM forward model predicts the CSDs of BOLD signals as:

$$G_y(\omega) = H(\omega)(i\omega I - A)^{-1}G_v(\omega) \cdot (-i\omega I - A^T)^{-1}H(\omega)^* + G_e(\omega) \quad (22)$$

### 3.4 Optimisation Techniques in DCM

Accurate parameter estimation is essential for fitting DCMs, but this is complicated by the models' high dimensionality, non-linear dynamics, and the inherent noise in fMRI data. As such, the choice of optimisation algorithm strongly impacts convergence reliability and model accuracy.

Grid search performs exhaustive evaluation over a predefined parameter grid, but becomes computationally infeasible as dimensionality increases, and lacks gradient guidance for efficient exploration [26].

AdamW, a modern gradient-based optimiser, adapts learning rates for individual parameters using first and second moment estimates, and incorporates decoupled weight decay to improve convergence and regularisation [27]. While effective in large parameter spaces, its performance depends on accurate gradient estimates and can be sensitive to local minima without careful initialisation.

Optuna, based on Bayesian optimisation via Tree-structured Parzen Estimators (TPEs), models the objective function probabilistically and selects new configurations to explore based on prior performance [28]. It requires no gradient information, making it well-suited for non-differentiable or computationally intensive models. Its flexibility and pruning strategies make it effective for DCMs with noisy or expensive objective evaluations. However, Bayesian optimisation can become inefficient in very high-dimensional search spaces, where the model struggles to accurately approximate the objective function [28].

## 4.0 Methods

### 4.1 Data Acquisition and Ethics

Data were sourced from a publicly available dataset provided by Carhart-Harris et al. [18]. Twenty healthy participants underwent two ses-

sions in a double-blind, within-subject design, receiving either  $75\mu\text{g}$  of LSD or PLCB. rs-fMRI scans (14 minutes) were acquired approximately 225 minutes post-infusion. One participant who did not complete scanning and four participants with excessive motion were excluded, leaving 15 subjects for analysis. Preprocessing was performed using standard neuroimaging pipelines, including FSL, AFNI, FreeSurfer, and ANTs, to minimise artefacts from motion and physiological noise.

The original study was approved by the National Research Ethics Service Committee London-West London and complied with the Declaration of Helsinki and Good Clinical Practice guidelines. All data were fully anonymised, and no new data collection or direct participant contact was involved in this study.

### 4.2 Implementation of P-DCM Model

P-DCM was implemented in PyTorch to simulate BOLD signals and evaluate parameter recovery under controlled conditions. Default parameter values, covering intrinsic neuronal connectivity, NVC, and haemodynamic model parameters, were adopted from Havlicek et al. [6], providing a physiologically grounded baseline.

The system of SDEs were solved using the Euler–Maruyama method, a first-order numerical technique that extends the classical Euler method by incorporating a noise term scaled by the square root of the time step [29]. This approach is well suited for simulating the evolution of noisy, non-linear dynamical systems driven by neural and vascular fluctuations.

To replicate endogenous variability, coloured noise with a power-law spectral profile  $\alpha \cdot f^{-\beta}$  was introduced into both the state dynamics and BOLD observations using a custom noise generator, capturing the characteristic  $1/f^\beta$  scaling observed in neural and vascular signals [30]. Independent noise components were defined for the state and observation processes, each characterised by its own spectral parameters  $(\alpha_v, \beta_v)$  and  $(\alpha_e, \beta_e)$ , respectively.

The estimated parameter set included neuronal parameters  $(\sigma, \mu, \lambda)$ , NVC terms  $(\phi, \varphi, \chi)$ , haemo-

dynamic parameters ( $\tau$ ,  $\tau_1$ ,  $\alpha$ ,  $E_0$ ), and spectral noise parameters ( $\alpha_v$ ,  $\beta_v$ ,  $\alpha_e$ ,  $\beta_e$ ).

Simulations were conducted at high temporal resolution (100 Hz; integration step  $h = 0.01$  s) for durations matching empirical recordings ( $T = 434$  s). To align with the empirical sampling rate ( $TR = 2$  s; 0.5 Hz), the simulated BOLD signals were downsampled post-simulation by a factor of 200, ensuring consistent temporal resolution and CSD lengths for spectral loss calculations.

Simulated and empirical BOLD time series were normalised to unit variance before PSD computation to prevent bias from differences in absolute signal power. Without normalisation, differences in absolute signal power—arising from scanner gain or physiological variability—could dominate the PSD, even if spectral shapes are similar. This step ensures comparability across conditions and subjects prior to statistical analysis [31].

### 4.3 Implementation of spDCM Model

The spDCM approach is based on the haemodynamic transfer function  $H(\omega)$  (Equation 18) and the spectral forward model  $G_y(\omega)$  (Equation 22) proposed by Novelli et al. [7][25].

Neuronal fluctuations were modelled as power-law noise, with separate spectral density functions defined for the state and observation processes. Each was parametrised by region-specific amplitude and spectral slope values, as described in Section 3.3.3. Using these definitions, the predicted CSD  $G_y(\omega)$  was computed as a function of the transfer function  $H(\omega)$ , the effective connectivity matrix  $A$ , and the noise spectra  $G_v(\omega)$  and  $G_e(\omega)$ . The resulting model output is a complex-valued CSD matrix that captures both the power spectra and coherence between regional BOLD signals in the frequency domain.

During model inversion, parameters jointly optimised included the effective connectivity matrix  $A$ ; NVC and haemodynamic parameters ( $\varphi, \phi, \chi, \tau, \tau_1, \alpha, E_0$ ); and spectral noise parameters ( $\alpha_v, \beta_v, \alpha_e, \beta_e$ ).

### 4.4 Implementation of the Optimisation Framework

Several optimisation strategies were evaluated prior to final model inversion, including stand-alone grid search, AdamW, and Optuna. Grid search proved computationally intractable due to the high dimensionality of the parameter space; for example, a 14-parameter model with five discrete values per parameter would require evaluating  $5^{14} = 6,103,515,625$  combinations. AdamW enabled efficient local convergence but lacked the global exploratory capability required for high-dimensional optimisation [32]. Optuna improved efficiency over grid search but occasionally converged prematurely due to the curse of dimensionality [33].

To mitigate these limitations, a hybrid two-stage optimisation pipeline was implemented. In the first stage, global exploration of the parameter space was performed using Optuna. Parameter ranges were constrained to  $\pm 0.5$  around literature baseline values to ensure physiological plausibility. For each ROI, subject, and condition, 100 Optuna trials were conducted to balance parameter space exploration with computational cost.

The best-performing parameter set from Optuna was then used to initialise local optimisation with AdamW in the second stage. Parameters were refined by minimising MSE between predicted and empirical PSD over a fixed number of training epochs. AdamW hyperparameters were set as follows: learning rate  $10^{-3}$ , weight decay  $10^{-3}$ , and decay factor  $\gamma = 0.99$ .

For P-DCM, training was limited to 100 epochs per ROI, subject, and condition due to the computational expense of numerically solving the SDEs. In contrast, spDCM employed a closed-form frequency-domain model, allowing up to 1500 training epochs per run.

The complete optimisation framework was implemented in PyTorch and parallelised using Python’s multiprocessing module, enabling concurrent model fitting across ROIs, subjects, and experimental conditions. This parallelisation was essential for maintaining scalability and practical runtimes across the full dataset. Figure 4.4 il-

lustrates the two-stage optimisation pipelines for P-DCM and spDCM.

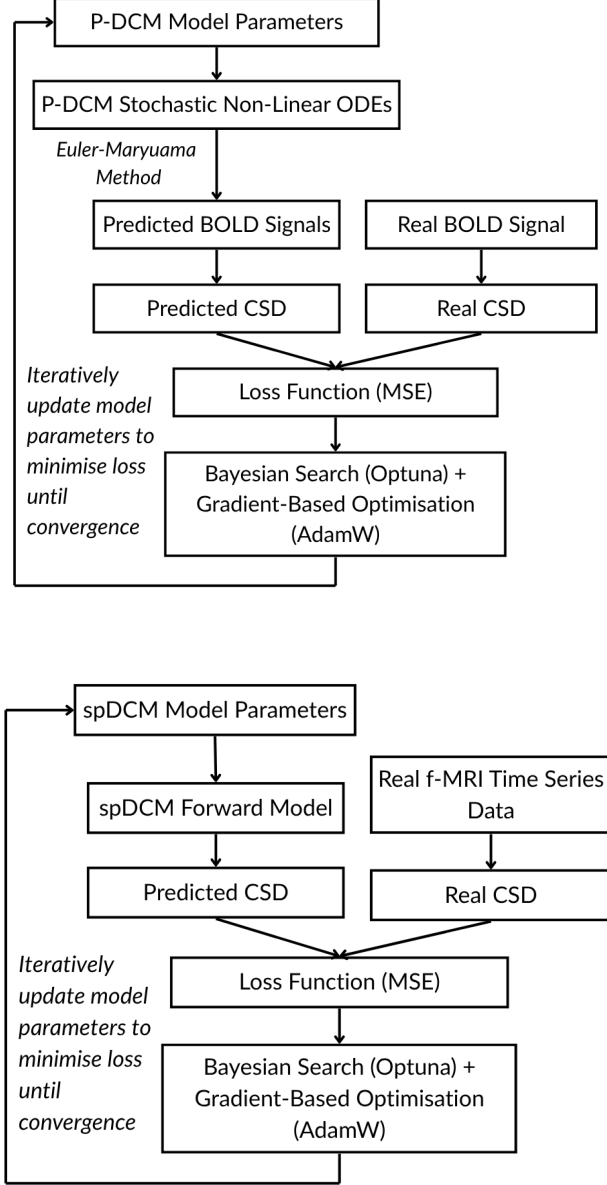


**Figure 2.** Optimisation pipelines. Top: P-DCM estimates parameters by minimising the mean squared error (MSE) between simulated and empirical rs-fMRI BOLD signal CSDs. Bottom: spDCM minimises the MSE between predicted ( $G_y(\omega)$ ) and empirical CSDs. Both pipelines use Optuna for global optimisation followed by AdamW refinement.

## 5.0 Results

### 5.1 Empirical vs Model-Predicted PSDs (PLCB Condition)

Figure 3 compares the PSDs of empirical and model-predicted BOLD signals for Subject 001, focusing on ROI 52 in the right hemisphere (RH) visual cortex, as defined by the 100-region Schaefer 2018 parcellation [34] (see Appendix A.2 for ROI-to-region mappings). The Schaefer atlas segments the cortex into functionally defined regions based on resting-state connectivity, enabling anatomically grounded comparisons. Analysis was restricted to the low-frequency band (0.01–0.1 Hz), where rs-fMRI exhibits dominant fluctuations reflecting intrinsic functional connectivity [35].

Real vs Recovered PSD for PLCB Condition

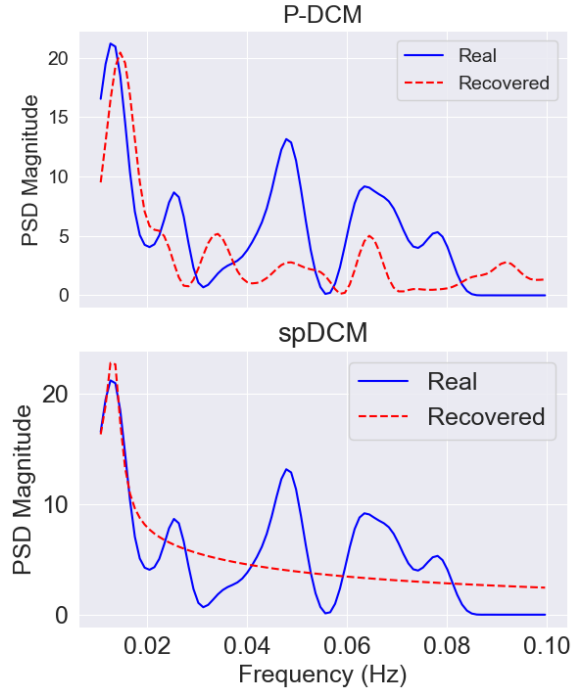


**Figure 3.** Comparison of real vs predicted PSDs for Subject 001 in ROI 52 under PLCB conditions using P-DCM and spDCM.

The P-DCM model more closely approximates the oscillatory structure of the empirical signal, despite some discrepancies in amplitude and spectral alignment. This suggests that P-DCM better captures dynamic neurovascular processes, likely due to its stochastic, time-domain formulation. In contrast, spDCM produces a smooth, uni-

modal spectrum with a single broad peak aligned with one of the empirical PSD maxima but fails to reproduce the multi-peaked structure observed in the real signal.

## 5.2 Model Comparisons: Efficiency and Fit Accuracy

To evaluate model performance, the distributions of fit times and normalised mean squared error (NMSE), which quantifies the deviation between predicted and empirical PSDs, were compared across all subjects, ROIs, and conditions for both P-DCM and spDCM. Figure 4 shows model runtime efficiency, while Figure 5 highlights fit accuracy.

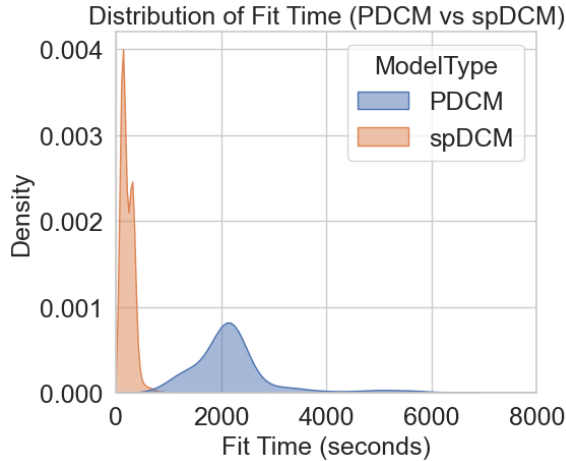


**Figure 4.** Distribution of Model Fit Times for P-DCM and spDCM.

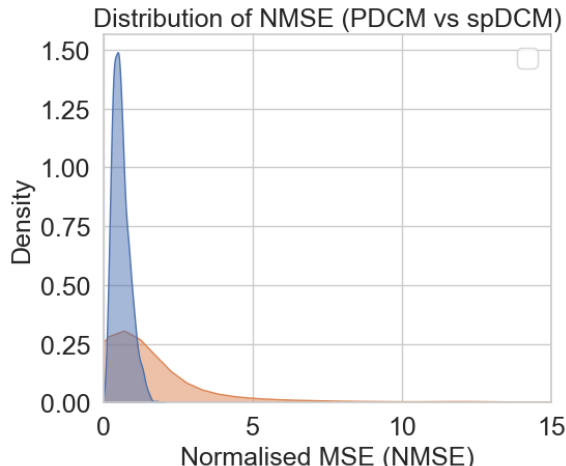


**Figure 5.** Distribution of NMSE for P-DCM and spDCM.

P-DCM exhibited significantly longer fit times,

ranging from 1,000 to over 6,000 seconds per fit due to the computational demands of solving SDEs at high temporal resolution. In contrast, spDCM, which employs a closed-form frequency-domain solution, completed most fits within a few hundred seconds, resulting in an average 11.2-fold reduction in fit time and substantial computational savings.

Across subjects and ROIs, P-DCM achieved a 55.94% lower NMSE on average compared to spDCM, indicating markedly improved recovery of the empirical spectral structure. The NMSE distribution for P-DCM was sharply peaked near zero, reflecting consistent fit quality, whereas spDCM showed a broader distribution with a heavier tail, indicating greater variability in fit accuracy across the dataset.

## 5.3 Performance Improvement Over Literature-Based Baselines

Model performance was further assessed by comparing optimised fits to literature-based parameter baselines: Havlicek et al. for P-DCM and Novelli et al. for spDCM. These baselines, while commonly referenced, were derived from different datasets and experimental conditions, and are therefore used as reference points for relative comparison rather than formal benchmarks for model validation. A complete listing of these baseline parameter values and plausible ranges is provided in Appendix A.1.

Fit improvements ( $\Delta$ ) were computed as optimised minus baseline values across six PSD-based metrics: three error measures (MSE, NMSE, relative error) and three similarity measures (explained variance, Pearson correlation, spectral coherence).

### *P-DCM Model*

P-DCM shows consistent improvements across all PSD-based metrics under the PLCB condition. The error-based metrics display narrow interquartile ranges and median values consistently below the baseline, indicating better alignment with the empirical PSD in both amplitude and spectral structure. The small number of outliers further suggests stable performance across sub-

jects and regions. Improvements in spectral similarity are similarly strong: median increases in explained variance, correlation, and coherence all exceed 0.2 across the dataset.

#### *spDCM Model*

In contrast, spDCM exhibits more variable performance across both error and similarity metrics. Error-based  $\Delta$  values tend to cluster around zero, with some fits showing limited or negative change. The broader spread and higher number of outliers suggest reduced consistency across ROIs and subjects.

Nonetheless, spDCM yields modest improvements in spectral similarity. Median increases in explained variance, correlation, and coherence are positive but smaller and more variable than those observed with P-DCM. This suggests that, while spDCM can enhance spectral alignment, its performance may be more sensitive to subject- or region-specific variability.

$\Delta$  (Fitted – Baseline) Performance Metrics: P-DCM vs spDCM

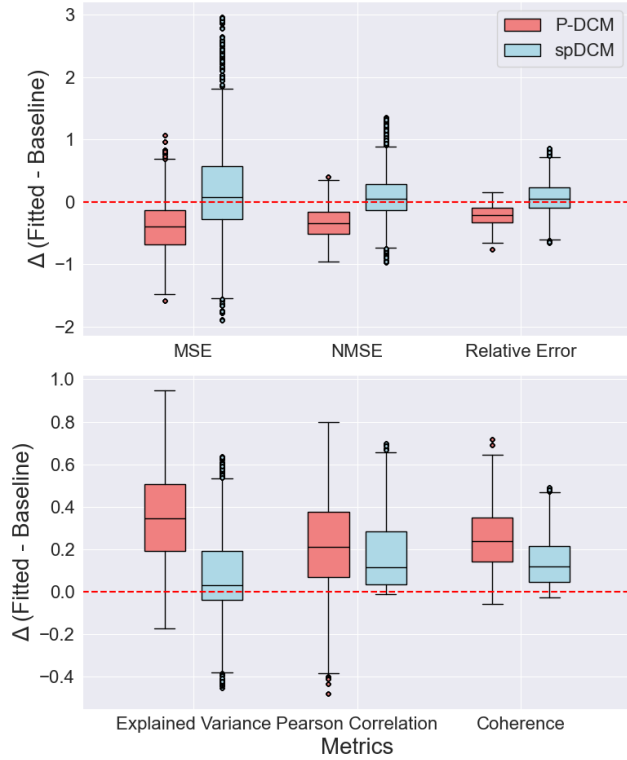


**Figure 6.** Improvements in model fit ( $\Delta$  = Fitted – Baseline) across six frequency-domain metrics for P-DCM and spDCM (PLCB condition)

#### 5.4 Parameter Correspondence Between P-DCM and spDCM

To assess the consistency of parameter estimates across models, Pearson correlation coefficients were computed for each shared parameter between P-DCM and spDCM under the PLCB condition. As detailed in Appendix A.3, all correlations were weak ( $|r| < 0.06$ ) and statistically non-significant ( $p > 0.06$ ).

The lack of statistically significant correlations, combined with near-zero effect sizes, suggests minimal linear correspondence between the parameter estimates produced by P-DCM and spDCM. This divergence does not imply model failure, but instead reflects the distinct computational architectures of the two frameworks. Differences in temporal resolution, stochastic modelling, and haemodynamic flexibility likely contribute to this discrepancy.

#### 5.5 Empirical vs Model-Predicted PSDs (LSD Condition)

Real vs Recovered PSD for LSD Condition

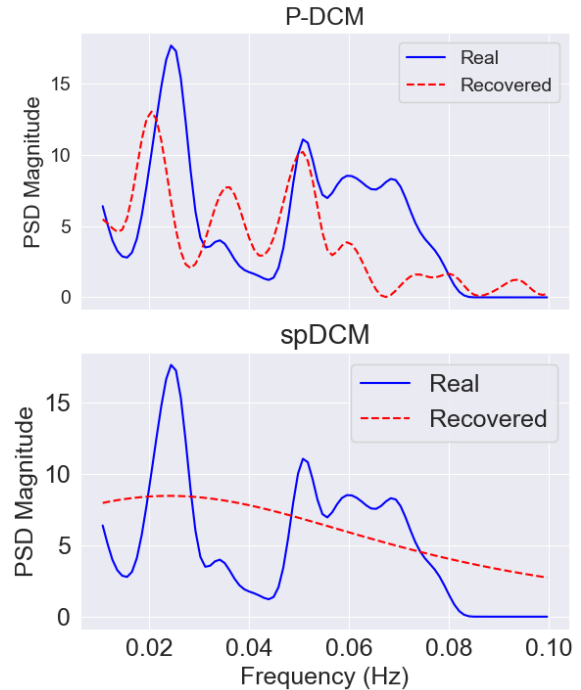


**Figure 7.** Comparison of real vs predicted PSDs for Subject 001 in ROI 52 under LSD conditions using P-DCM and spDCM models.

Figure 6 illustrates how P-DCM and spDCM perform under the LSD-induced state, again focusing on Subject 001 and ROI 52.

P-DCM continues to approximate key features of the empirical spectrum, capturing multiple low-frequency oscillations. However, some peak locations are still misaligned, and overall power is attenuated, as was also observed under the PLCB condition.

In contrast, spDCM yields a smoother, less structured spectrum that deviates more markedly from the empirical signal than under PLCB. The absence of distinct spectral peaks suggests limited capacity to model the increased spectral complexity characteristic of psychedelic states, highlighting the limitations of fixed-form, frequency-domain models in non-stationary regimes.

### 5.6 Cortical Surface Mapping of LSD-Induced Parameter Changes

Cortical surface maps were generated for all estimated parameters from P-DCM and spDCM using the *surfplot* package in Python [36][37] to examine the spatial distribution of LSD-induced neurovascular changes. As a representative case, results for the neurovascular gain parameter  $\phi$  are shown. Paired *t*-tests were performed across subjects for each ROI, comparing LSD and PLCB conditions. Figure 8 presents uncorrected surface maps of  $-\log_{10}(p)$ , *t*-statistics, and Cohen's *d*, reflecting the statistical significance, direction, and effect size of LSD-induced changes.

#### P-DCM Model

P-DCM identified eight cortical parcels with significant LSD-related modulation of  $\phi$ , spanning both hemispheres and including sensory and associative cortices. Increases in neurovascular gain were localised to regions responsible for vision and attention—namely, the lateral occipital and dorsal parietal areas. These areas belong to the visual and dorsal attention networks, respectively, with effect sizes up to  $d = 1.07$  and *t*-values reaching 3.38. These results suggest enhanced vascular responsiveness in sensory and attentional systems under LSD.

Conversely, pronounced decreases in  $\phi$  were

observed in transmodal associative regions, notably within the medial prefrontal and posterior cingulate cortices of the DMN, with *t*-values as low as  $-4.67$  and  $d = -1.48$ . This pattern suggests reduced vascular gain in areas associated with self-referential and integrative processing. The opposing effects across networks indicate spatially specific reorganisation of neurovascular responsiveness, rather than a global increase or decrease.

Surface Maps for LSD vs PLCB - Parameter: phi

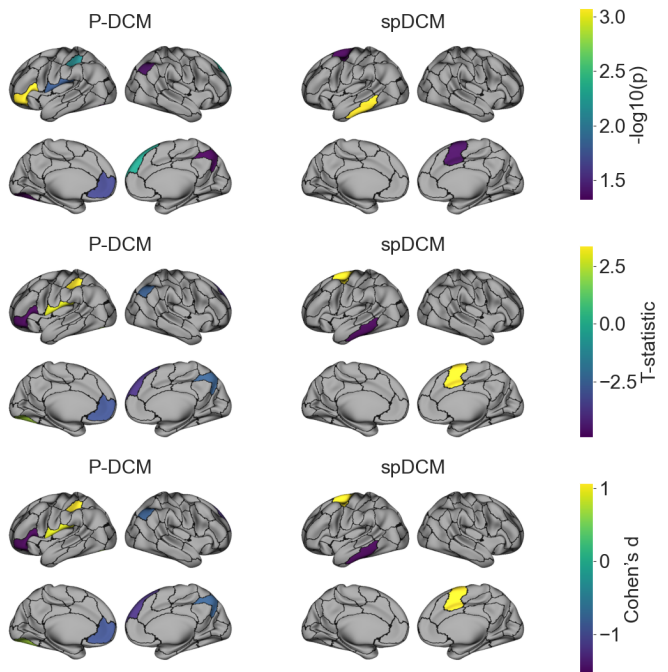


**Figure 8.** Surface maps of statistical comparisons for parameter  $\phi$  between LSD and PLCB. Top:  $-\log_{10}(p)$ ; Middle: *t*-statistics; Bottom: Cohen's *d*. Left: P-DCM; Right: spDCM. Highlighted ROIs exceed  $p < 0.05$  ( $-\log_{10}(p) > 1.3$ ).

#### spDCM Model

spDCM identified fewer significant effects, but with a similar directional pattern. Increases in  $\phi$  were observed in the left hemisphere (LH) frontal eye field (dorsal attention network) and RH salience cortex, with effect sizes exceeding  $d = 0.78$ . A strong decrease was found in the LH temporal pole (limbic network;  $t = -4.90$ ,  $d = -1.55$ ), a region implicated in emotional and self-referential processing. This aligns with P-

DCM findings, which also showed reduced vascular gain in both DMN region (e.g., mPFC, PCC) and limbic regions (e.g., temporal pole), consistent with disrupted self-referential and affective processing under LSD. Although the spatial extent was more limited in spDCM, the consistent directionality across networks suggests converging neurovascular effects between models.

Although several regions reached statistical significance, none survived correction for multiple comparisons (Bonferroni-Holm, or False Discovery Rate (FDR)), likely due to small sample size and conservative thresholds.

## 5.7 Network-Level Statistical Mapping of Parameter Changes

To characterise LSD-related changes at the network level, uncorrected paired *t*-tests were computed for each parameter–network pair using P-DCM estimates. The resulting  $-\log_{10}(p)$  values are visualised in hierarchically clustered heatmaps for both P-DCM and spDCM (Figure 9).

### P-DCM Model

Twelve parameter–network pairs showed uncorrected effects at  $p < 0.05$  (Appendix A.5). The strongest effect was for  $\alpha$  in the RH DMN ( $t = 3.35, d = 1.01$ ), with similar excitability increases in  $\alpha_e$  for the RH limbic ( $t = 2.80, d = 0.81$ ) and RH DMN ( $t = 2.45, d = 0.74$ ). In contrast,  $\alpha_e$  was reduced in the LH control network ( $t = -2.95, d = -0.76$ ).

The neurovascular gain parameter  $\phi$  was elevated in the LH salience ( $t = 2.99, d = 0.77$ ) and LH dorsal attention ( $t = 2.39, d = 0.62$ ) networks, indicating increased coupling strength. Vascular inflow  $\chi$  increased in the LH control ( $t = 2.31$ ), LH DMN ( $t = 2.26$ ), and RH visual ( $t = 2.73$ ) networks. Small but significant decreases in  $E_0$  (oxygen extraction) and  $\alpha_v$  (state noise) were observed in the RH visual and RH somatomotor networks, respectively ( $t = -2.16$  for both,  $d = -0.56$ ).

Hierarchical clustering of *t*-statistics and effect sizes revealed three stable parameter groupings:  $(\alpha, \alpha_e)$  related to excitability and observation gain;  $(\alpha_v, \phi)$  associated with state noise and vasoactive decay; and  $(E_0, \chi, \phi)$  reflecting vascu-

lar and metabolic regulation.

Three network clusters were also identified: (RH and LH control, RH DMN), (LH dorsal attention, LH salience), and (RH visual, LH DMN), suggesting coordinated physiological changes across associative, attentional, and sensory networks. However, none of these effects remained significant after Bonferroni–Holm or FDR correction, and results should be interpreted as exploratory.

### spDCM Model

Ten parameter–network pairs showed uncorrected effects at the  $p < 0.05$  threshold (Appendix A.5). The most prominent effects involved observation and state noise, as well as connectivity-related parameters.  $\alpha_e$  was significantly increased in the LH salience ( $t = 2.96, d = 0.76$ ), LH limbic, and RH somatomotor networks.  $A_{\text{imag}}$  was elevated in the LH DMN ( $t = 2.83, d = 0.73$ ), suggesting altered inter-regional phase relationships.  $\alpha_v$  also increased in the LH dorsal attention network ( $t = 2.35, d = 0.61$ ).

Conversely, reductions were observed in several physiological parameters.  $\beta_e$  decreased in the RH limbic network ( $t = -2.42, d = -0.63$ ), potentially reflecting changes in observation noise slope. Declines in  $\tau_1$  and  $\chi$  were found in the RH dorsal attention ( $t = -2.40, d = -0.62$ ) and LH somatomotor networks ( $t = -2.36, d = -0.61$ ), respectively.  $\alpha$  decreased in the RH DMN ( $t = -2.34, d = -0.60$ ), while a slight increase in  $\tau$  was observed in the RH visual cortex ( $t = 2.15, d = 0.56$ ).

Clustering of *t*-statistics and effect sizes revealed two main parameter groupings:  $(\alpha, \chi)$ , linked to vascular tone and neural gain, and  $(\tau, \tau_1)$ , reflecting synaptic and haemodynamic timing. Three network clusters also emerged: (1) RH visual and RH dorsal attention, (2) LH somatomotor and RH limbic, and (3) LH salience, RH somatomotor, and ventral attention. These patterns suggest LSD-related system-level modulation across sensorimotor and associative networks. As with P-DCM, none of the effects survived correction for multiple comparisons and should be interpreted with caution.

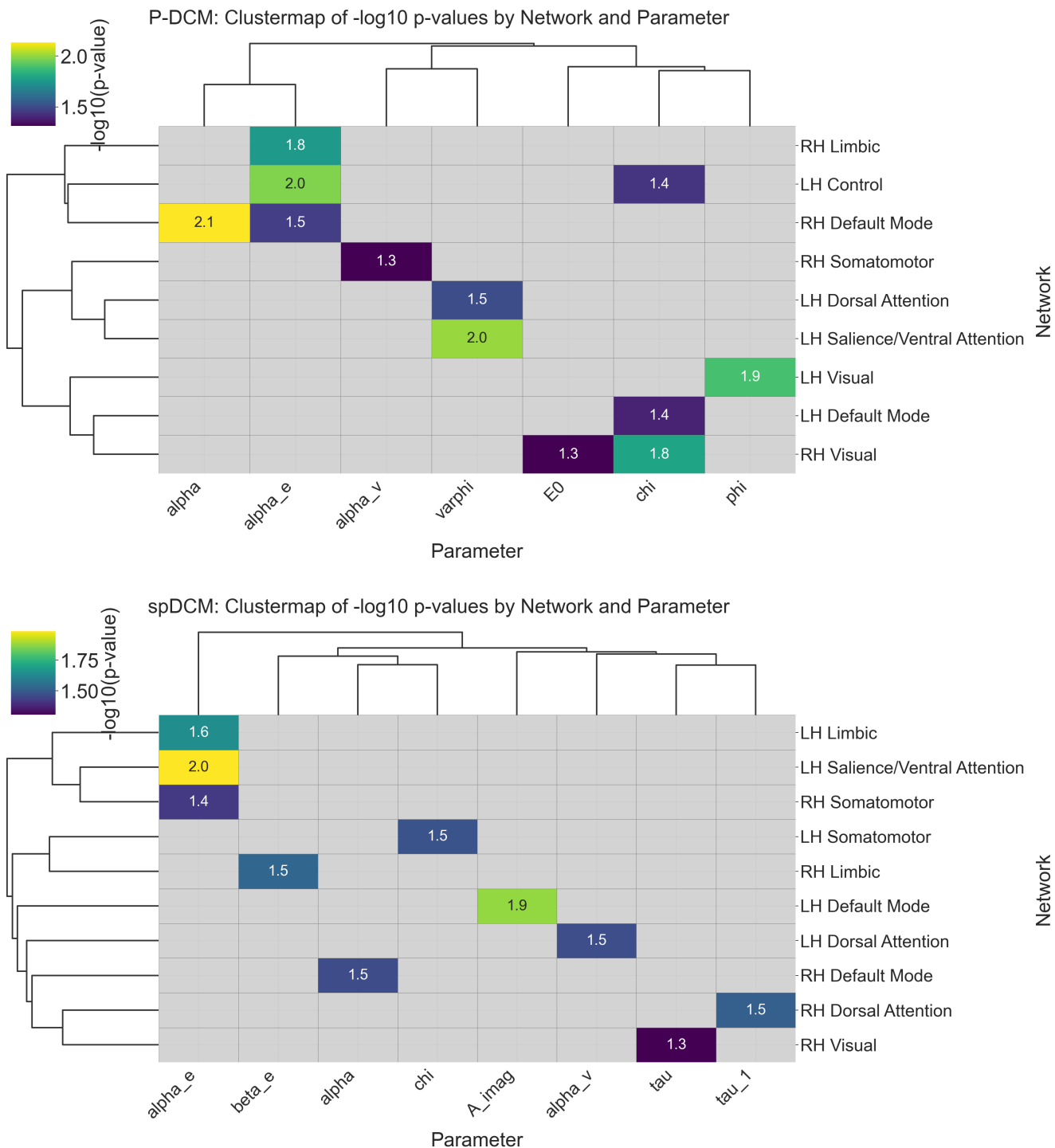


**Figure 9.** Network-level  $-\log_{10}(p)$  values from uncorrected paired  $t$ -tests comparing LSD and PLCB conditions for P-DCM (top) and spDCM (bottom) parameters. Values above 1.3 correspond to uncorrected  $p < 0.05$ .

## 5.8 Univariate Cluster-Based Permutation Testing (Per-Parameter Across ROIs)

To identify LSD-induced changes in individual physiological parameters, a univariate cluster-based permutation test was applied *separately* for each parameter across cortical ROIs. This method assesses whether a single parameter shows consistent effects in spatially contiguous regions.

Standard multiple comparison corrections (e.g., Bonferroni, FDR) can be overly conservative when testing many ROIs, reducing sensitivity to spatially extended effects. In contrast, cluster-based testing improves sensitivity by leveraging the assumption that biologically meaningful changes tend to occur in anatomical clusters rather than isolated areas [38].

For each parameter, within-subject difference scores (LSD minus PLCB) were computed across all ROIs. A one-sample cluster-based permutation test was then performed using the `permutation_cluster_1samp_test` function from MNE-Python. Clusters were defined as anatomically adjacent ROIs based on Schaefer atlas groupings. To assess statistical significance, 5,000 permutations were conducted in which the sign of each subject's difference score was randomly flipped, simulating the null hypothesis of no systematic effect. For each permutation, the maximum cluster-level statistic (the sum of  $t$ -values within each cluster) was recorded to build a null distribution. Observed clusters were deemed significant if their statistic exceeded the 95th percentile of this distribution, corresponding to a family-wise error (FWE)-corrected threshold of  $p < 0.05$ .

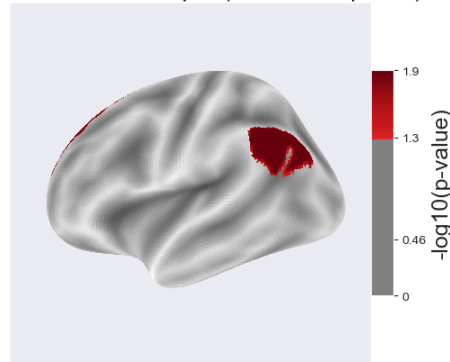
### P-DCM Model

Univariate testing revealed one significant cluster for each of four parameters, comprising anatomically and functionally adjacent ROIs with consistent LSD–PLCB differences (Table 1).

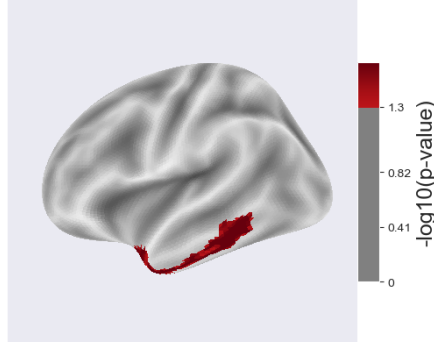
$\tau$  formed a positive cluster in the anterior insula and medial prefrontal cortex ( $t > 2.5$ ), regions associated with the salience network. This may reflect a more prolonged or sustained vascular response under LSD.

$\beta_v$ , reflecting the spectral slope of endogenous

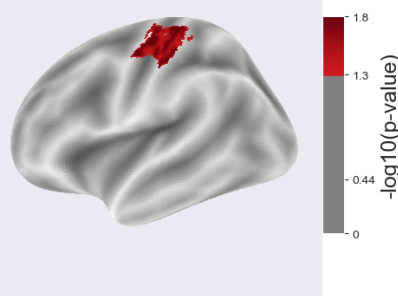
Significant ROIs for phi (Left Hemisphere)



Significant ROIs for tau\_1 (Left Hemisphere)



Significant ROIs for beta\_v (Left Hemisphere)



Significant ROIs for sigma (Left Hemisphere)

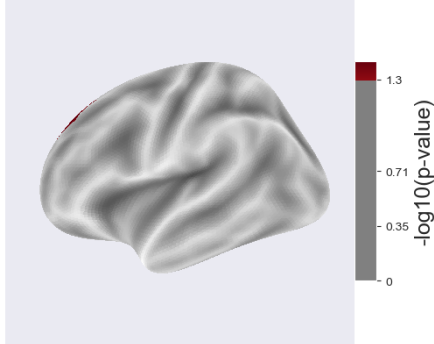


**Figure 10.** P-DCM: Surface maps of significant ROIs for  $\phi$ ,  $\tau_1$ ,  $\beta_v$ ,  $\sigma$ . Colours represent  $-\log_{10}(p)$  values from permutation tests with threshold of  $p < 0.05$ .

fluctuations, showed a negative cluster in the LH visual cortex ( $t < -2.8$ ), suggesting reduced low-frequency power in spontaneous activity.

$\phi$ , which governs the gain of the neurovascular response, showed a negative cluster across posterior DMN regions ( $t < -2.2$ ), consistent with attenuated vascular responsiveness under LSD.

Surface projections of these clusters are shown in Figure 10.

**Table 1**

Significant clusters from P-DCM permutation testing (FWE-corrected,  $p < 0.05$ ).

Parameter	ROI	t-value	p (cluster)
$\tau$	28	4.26	0.0234
$\tau$	29	2.56	0.0234
$\beta_v$	4	-3.35	0.0168
$\beta_v$	7	-2.83	0.0168
$\sigma$	43	2.17	0.0384
$\sigma$	48	4.05	0.0384
$\phi$	39	-2.30	0.0140
$\phi$	42	-2.26	0.0140
$\phi$	43	-3.11	0.0140

### spDCM Model

Permutation-based cluster correction revealed a single significant cluster in the imaginary component of the effective connectivity matrix ( $A_{\text{imag}}$ ), spanning ROIs 42, 43, and 49 ( $p = 0.0258$ ; shown in Figure 11 and Table 2).

**Table 2**

Significant clusters from spDCM permutation testing (FWE-corrected,  $p < 0.05$ )

Parameter	ROI	t-value	p (cluster)
$A_{\text{imag}}$	42	2.19	0.0258
$A_{\text{imag}}$	43	2.34	0.0258
$A_{\text{imag}}$	49	3.54	0.0258

All three regions are located within the left-lateralised DMN, suggesting that LSD modulates the phase component of inter-regional connectivity within this system. The positive  $t$ -values ( $t =$

2.19 to 3.54) indicate consistent increases in the imaginary component of connectivity under LSD relative to PLCB, which may reflect enhanced phase-lagged synchronisation among DMN regions. This is consistent with previous findings of disrupted temporal coordination in resting-state activity during psychedelic states [18].

Significant ROIs for  $A_{\text{imag}}$  (Left Hemisphere)

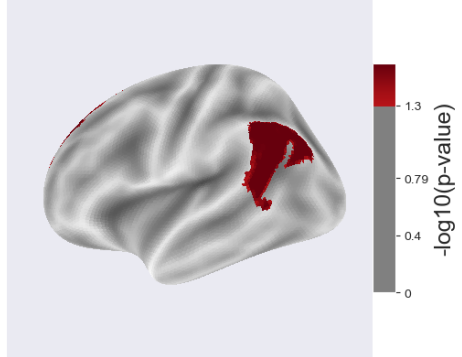


**Figure 11.** spDCM: Surface maps of significant ROIs for  $A_{\text{imag}}$ .

### 5.9 Multi-Dimensional Cluster-Based Permutation Testing (Parameter $\times$ ROI)

While the univariate analysis tests each parameter separately, the multidimensional test evaluates all parameter-ROI pairs together within a joint framework. Each pair is treated as a point in a 2D grid (parameter  $\times$  ROI), with clustering based on spatial adjacency among ROIs as defined by the Schaefer atlas as well. This allows for the detection of distributed but consistent effects that may not reach significance in separate, per-parameter tests.

Clusters were defined solely by spatial adjacency among ROIs within each parameter, using anatomical neighbourhood groupings from the Schaefer parcellation. No similarity or adjacency was assumed between parameters, which were treated as independent. This design increases sensitivity to subtle LSD-induced changes that may be weak within individual parameters but show consistent modulation across adjacent brain regions in the broader physiological feature space.

As with the univariate test, 5,000 sign-flip permutations were used to assess significance. This

approach complements the univariate analysis by increasing sensitivity to system-level effects spanning multiple physiological processes and brain regions.

**Table 3**

Multi-dimensional cluster-based permutation results across parameter-ROI space.

Model	Result
P-DCM	67 clusters identified. Significant: $\sigma$ in ROIs 43 ( $t = 2.39$ ), 48 ( $t = 6.51$ ), 49 ( $t = 2.78$ ); $p = 0.0254$ .
spDCM	52 clusters identified. No significant clusters detected.

#### *P-DCM Model*

In the P-DCM model, 67 clusters were identified across the parameter-ROI space. One statistically significant cluster emerged for the excitatory self-connection parameter  $\sigma$  ( $p = 0.0254$ ), as seen in Table 3, spanning three spatially adjacent ROIs in the LH DMN ( $t = 2.39$  to  $6.51$ ). This reflects a consistent reduction in local self-inhibition, implying increased excitability or signal variability within medial prefrontal and posterior cingulate cortices. These regions are core hubs of the DMN, and such changes align with theories suggesting that psychedelic states involve a destabilisation of intrinsic networks through reduced inhibitory control [18].

#### *spDCM Model*

For the spDCM model, a total of 52 thresholded clusters were identified based on spatial adjacency within parameters. However, none exceeded the corrected significance threshold, indicating that the observed effects did not form spatially coherent patterns that exceeded the permutation-based significance threshold. This suggests that LSD-induced changes estimated by spDCM may be more spatially localised, lower in magnitude, or affected by greater inter-subject variability, limiting the emergence of consistent parameter-region clusters in this model.

## 6.0 Discussion

This study compared P-DCM and spDCM in modelling resting-state fMRI spectral features and LSD-induced changes in inferred neurovascular and neuronal dynamics. P-DCM’s detailed time-domain modelling of NVC and stochastic neural fluctuations enabled it to capture the complex spectral structure of empirical data, characterised by a broad low-frequency peak with embedded oscillatory components. This resulted in consistently lower NMSE values and more stable parameter estimates across subjects and regions. In contrast, spDCM’s stationary, frequency-domain formulation produced spectra with a single dominant peak and otherwise smooth structure, failing to capture the additional low-frequency oscillatory components observed in the empirical signal.

Although grounded in similar biophysical principles, P-DCM and spDCM yielded effectively uncorrelated parameter estimates under the PLCB condition. This divergence likely reflects differences in how each model represents neural and haemodynamic dynamics, reinforcing the need for model-specific interpretation rather than direct comparison. As a result, parameter values derived from one model may not map directly onto those from the other. Apparent discrepancies caution against assuming one-to-one correspondence between models and underscore the importance of model-specific interpretation when drawing inferences from estimated parameters.

Under LSD, the divergence between models became more pronounced. P-DCM retained its sensitivity to the richer spectral dynamics of the altered state, capturing multiple low-frequency oscillations characteristic of psychedelic neurophysiology. In contrast, spDCM continued to yield spectra dominated by a single broad peak, but with reduced amplitude and a flatter profile—further limiting its ability to reflect the increased nonlinearity and non-stationarity induced by LSD. This highlights spDCM’s diminished suitability for modelling the increased nonlinearity and non-stationarity induced by psychedelic perturbation.

Spatially, LSD effects were regionally specific rather than uniform. Increases in neurovascular gain were concentrated in sensory and attention-related areas, while associative networks such as the DMN exhibited decreased gain. This spatial pattern aligns with previous findings suggesting that psychedelics reallocate cortical processing from high-level integrative functions toward enhanced bottom-up sensory responsivity. P-DCM identified a broader and more spatially coherent pattern of changes compared to spDCM, likely due to its finer temporal resolution and explicit modelling of stochastic dynamics.

While no network-level *t*-tests survived correction for multiple comparisons, cluster-based permutation analyses in P-DCM identified significant spatial clusters, particularly within pre-frontal and default mode regions. These involved parameters related to oxygen metabolism and excitatory-inhibitory balance, suggesting spatially structured physiological effects under LSD. In contrast, spDCM detected one significant univariate cluster in the imaginary connectivity component but failed to identify significant clusters in the multidimensional analysis, likely due to greater inter-subject variability and reduced sensitivity to distributed physiological changes spanning multiple regions and parameters.

## 6.1 Limitations and Constraints

### 1. Physiological Assumptions in P-DCM.

P-DCM assumes that CBF is a smoothed, positively constrained convolution of neuronal activity, omitting negative feedback mechanisms in NVC that could produce transient CBF dynamics. While this improves interpretability and aligns with typical physiology, it cannot account for non-neural low-frequency oscillations (e.g., Mayer waves), which may influence resting-state signal variance [6].

The model also assumes tight coupling between CBF and CMRO<sub>2</sub> during both steady-state and transient periods, based on the oxygen-limitation model and experimental support [1]. However, some evidence suggests that oxygen metabolism and CBF may

exhibit different temporal dynamics, particularly during the post-stimulus BOLD undershoot [9][20]. Given that CMRO<sub>2</sub> and CBV effects are largely interchangeable in the BOLD signal, and that CMRO<sub>2</sub> cannot yet be measured directly at high temporal resolution, P-DCM models only one of these mechanisms. While practical, this limits the model's ability to represent dissociations between flow and metabolism.

### 2. Modelling Simplifications in spDCM.

spDCM was applied at the single-region level, modelling only within-region parameter changes. This simplification omits inter-regional effective connectivity, which may be especially important under psychedelics. In addition, spDCM assumes fixed haemodynamics and temporal stationarity [7], limiting its ability to capture nonlinear or time-varying effects induced by LSD. Although several strong local effects were observed, their lack of spatial consistency likely contributed to the absence of significant clusters, indicating high sensitivity to inter-subject variability.

### 3. Fixed Cortical Parcellations.

Using standard anatomical atlases assumes consistent brain organisation across individuals and may miss subject-specific functional reconfigurations induced by LSD.

### 4. Baseline Parameters and Validation.

Baseline parameter estimates were drawn from previous studies, which may not fully capture the characteristics of this dataset. Furthermore, in the absence of direct biological validation, inferences about physiological mechanisms remain indirect. Some observed differences may reflect adaptation from suboptimal baselines rather than genuine neurophysiological change.

## 6.2 Future Work

Future research could explore neural network-based modelling frameworks to better capture physiological dynamics while reducing computational demands. For example, PINNs incorporate biophysical constraints into learning,

enabling physiologically plausible and efficient parameter estimation [8]. DeepONets can model complex nonlinear parameter interactions, offering scalable inversion strategies [9]. Integrating multimodal data—such as EEG or CBF—may further improve parameter estimation and reduce reliance on fixed haemodynamic assumptions. Expanding datasets to include task-based paradigms will also be important for testing model generalisability and disentangling the distinct neural and vascular effects of psychedelics. Finally, analysing CSDs may enhance the modelling of inter-regional functional interactions, complementing the within-region spectral focus of the present study.

## 7.0 Conclusion

This study evaluated two generative modelling approaches—P-DCM and spDCM—for characterising LSD-induced changes in rs-fMRI. By explicitly modelling stochastic neural dynamics and NVC in the time domain, P-DCM more accurately captured the low-frequency spectral structure characteristic of psychedelic states, outperforming spDCM in model fit, parameter stability, and sensitivity to spatially coherent effects. P-DCM identified LSD-related changes in parameters governing excitability, vascular inflow, and metabolic coupling, predominantly within visual, salience, and default mode networks—consistent with a shift from high-level integrative processing toward enhanced sensory responsiveness. In contrast, spDCM detected only isolated, uncorrected effects and lacked sensitivity under permutation-based cluster inference, highlighting limitations in modelling the non-stationary and non-linear dynamics of psychedelic states. Despite higher computational demands, P-DCM’s enhanced biophysical interpretability and sensitivity of network- and parameter-specific changes underscores the importance of physiologically grounded frameworks that accommodate dynamic neural complexity in psychedelic neuroimaging.

## References

- [1] R. e. a. Buxton, “Modeling the hemodynamic response to brain activation,” *NeuroImage*, vol. 23, S220–S233, 2004. doi: 10.1016/j.neuroimage.2004.07.013.
- [2] M. Lee, C. Smyser, and J. Shimony, “Resting-state fmri: A review of methods and clinical applications,” *American Journal of Neuroradiology*, vol. 34, no. 10, pp. 1866–1872, 2012. doi: 10.3174/ajnr.a3263.
- [3] D. e. a. De Gregorio, “Hallucinogens in mental health: Preclinical and clinical studies on lsd, psilocybin, mdma, and ketamine,” *Journal of Neuroscience*, vol. 41, no. 5, pp. 891–900, 2020. doi: 10.1523/jneurosci.1659–20.2020.
- [4] A. e. a. Luppi, “Lsd alters dynamic integration and segregation in the human brain,” *NeuroImage*, vol. 227, p. 117653, 2020. doi: 10.1016/j.neuroimage.2020.117653.
- [5] J. e. a. Fuentes, “Therapeutic use of lsd in psychiatry: A systematic review of randomized-controlled clinical trials,” *Frontiers in Psychiatry*, vol. 10, 2020. doi: 10.3389/fpsyg.2019.00943.
- [6] M. e. a. Havlicek, “Physiologically informed dynamic causal modeling of fmri data,” *NeuroImage*, vol. 122, pp. 355–372, 2015. doi: 10.1016/j.neuroimage.2015.07.078.
- [7] L. Novelli, K. Friston, and A. Razi, “Spectral dynamic causal modeling: A didactic introduction and its relationship with functional connectivity,” *Network Neuroscience*, vol. 8, no. 1, pp. 178–202, 2023. doi: 10.1162/netn\_a\_00348.
- [8] M. Raissi, P. Perdikaris, and G. Karniadakis, “Physics-informed neural networks: A deep learning framework for solving forward and inverse problems involving nonlinear partial differential equations,” *Journal of Computational Physics*,

- vol. 378, pp. 686–707, 2018. doi: 10.1016/j.jcp.2018.10.045.
- [9] L. e. a. Lu, “Learning nonlinear operators via deeponet based on the universal approximation theorem of operators,” *Nature Machine Intelligence*, vol. 3, no. 3, pp. 218–229, 2021. doi: 10.1038/s42256-021-00302-5.
- [10] G. Glover, “Overview of functional magnetic resonance imaging,” *Neurosurgery Clinics of North America*, vol. 22, no. 2, pp. 133–139, 2011. doi: 10.1016/j.nec.2010.11.001.
- [11] K. e. a. Kwong, “Dynamic magnetic resonance imaging of human brain activity during primary sensory stimulation,” *Proceedings of the National Academy of Sciences*, vol. 89, no. 12, pp. 5675–5679, 1992. doi: 10.1073/pnas.89.12.5675.
- [12] M. Noseworthy, D. Bulte, and J. Alfonsi, “Bold magnetic resonance imaging of skeletal muscle,” *Seminars in Musculoskeletal Radiology*, vol. 7, no. 4, pp. 307–316, 2003. doi: 10.1055/s-2004-815678.
- [13] K. Uludağ, B. Müller-Bierl, and K. Uğurbil, “An integrative model for neuronal activity-induced signal changes for gradient and spin echo functional imaging,” *NeuroImage*, vol. 48, no. 1, pp. 150–165, 2009. doi: 10.1016/j.neuroimage.2009.05.051.
- [14] C. Chang, J. Cunningham, and G. Glover, “Influence of heart rate on the bold signal: The cardiac response function,” *NeuroImage*, vol. 44, no. 3, pp. 857–869, 2008. doi: 10.1016/j.neuroimage.2008.09.029.
- [15] L. e. a. Shi, “Brain entropy is associated with divergent thinking,” *Cerebral Cortex*, 2019. doi: 10.1093/cercor/bhz120.
- [16] E. e. a. Tagliazucchi, “Increased global functional connectivity correlates with lsd-induced ego dissolution,” *Current Biology*, vol. 26, no. 8, pp. 1043–1050, 2016. doi: 10.1016/j.cub.2016.02.010.
- [17] R. e. a. Carhart-Harris, “The entropic brain: A theory of conscious states informed by neuroimaging research with psychedelic drugs,” *Frontiers in Human Neuroscience*, vol. 8, 2014. doi: 10.3389/fnhum.2014.00020.
- [18] R. e. a. Carhart-Harris, “Neural correlates of the lsd experience revealed by multimodal neuroimaging,” *Proceedings of the National Academy of Sciences*, vol. 113, no. 17, pp. 4853–4858, 2016. doi: 10.1073/pnas.1518377113.
- [19] M. e. a. Schartner, “Increased spontaneous meg signal diversity for psychoactive doses of ketamine, lsd and psilocybin,” *Scientific Reports*, vol. 7, no. 1, 2017. doi: 10.1038/srep46421.
- [20] M. Veldsman, T. Cumming, and A. Brodtmann, “Beyond bold: Optimizing functional imaging in stroke populations,” *Human Brain Mapping*, vol. 36, no. 4, pp. 1620–1636, Apr. 2015, Epub 2014 Dec 2. doi: 10.1002/hbm.22711.
- [21] A. Wsół, “Cardiovascular safety of psychedelic medicine: Current status and future directions,” *Pharmacological Reports*, vol. 75, pp. 1362–1380, 2023. doi: 10.1007/s43440-023-00539-4. [Online]. Available: <https://doi.org/10.1007/s43440-023-00539-4>.
- [22] M. E. Liechti, “Modern clinical research on lsd,” *Neuropsychopharmacology*, vol. 42, no. 11, pp. 2114–2127, Oct. 2017, Epub 2017 Apr 27. doi: 10.1038/npp.2017.86.
- [23] K. e. a. Stephan, “Comparing hemodynamic models with dcm,” *NeuroImage*, vol. 38, no. 3, pp. 387–401, 2007. doi: 10.1016/j.neuroimage.2007.07.040.
- [24] R. B. Buxton, E. C. Wong, and L. R. Frank, “Dynamics of blood flow and oxy-

- genation changes during brain activation: The balloon model,” *Magnetic Resonance in Medicine*, vol. 39, no. 6, pp. 855–864, Jun. 1998. doi: 10.1002/mrm.1910390602.
- [25] L. e. a. Novelli, “Minimum-phase property of the hemodynamic response function, and implications for granger causality in fmri,” *arXiv*, 2023. doi: 10.48550/arxiv.2312.01833.
- [26] P. Liashchynskyi and P. Liashchynskyi, “Grid search, random search, genetic algorithm: A big comparison for nas,” *arXiv preprint arXiv:1912.06059*, 2019.
- [27] Z. Zhuang *et al.*, “Understanding adamw through proximal methods and scale-freeness,” *arXiv preprint arXiv:2202.00089*, 2022.
- [28] T. Akiba, S. Sano, T. Yanase, T. Ohta, and M. Koyama, “Optuna: A next-generation hyperparameter optimization framework,” in *Proceedings of the 25th ACM SIGKDD International Conference on Knowledge Discovery & Data Mining*, ACM, 2019, pp. 2623–2631.
- [29] W. Liu and X. Mao, “Strong convergence of the stopped euler–maruyama method for nonlinear stochastic differential equations,” *Applied Mathematics and Computation*, vol. 223, pp. 389–400, 2013.
- [30] M. Stoyanov, M. Gunzburger, and J. Burkardt, “Pink noise, 1/fnoise, and their effect on solutions of differential equations,” *International Journal for Uncertainty Quantification*, vol. 1, no. 3, pp. 257–278, 2011. doi: 10.1615/int.j.uncertaintyquantification.2011003089.
- [31] A. Nieto-Castanon, “Preparing fmri data for statistical analysis,” in *fMRI Techniques and Protocols*, ser. Neuromethods, M. Filippi, Ed., vol. 220, Published May 31, 2025, New York, NY: Humana, 2025, Chapter 6, ISBN: 978-1-0716-4437-9. doi: 10.1007/978-1-0716-4438-6\_6. [Online]. Available: [https://doi.org/10.1007/978-1-0716-4438-6\\_6](https://doi.org/10.1007/978-1-0716-4438-6_6).
- [32] S. J. Reddi, S. Kale, and S. Kumar, “On the convergence of adam and beyond,” *arXiv preprint arXiv:1904.09237*, 2019.
- [33] J. Huang and D. Zhan, “An adaptive dropout approach for high-dimensional bayesian optimization,” *arXiv preprint arXiv:2504.11353*, 2025. arXiv: 2504.11353.
- [34] A. Schaefer, R. Kong, E. M. Gordon, *et al.*, “Local-global parcellation of the human cerebral cortex from intrinsic functional connectivity mri,” *Cerebral Cortex*, vol. 28, no. 9, pp. 3095–3114, Sep. 2018. doi: 10.1093/cercor/bhx179.
- [35] Y. e. a. Ao, “Intrinsic neural timescales relate to the dynamics of infraslow neural waves,” *NeuroImage*, vol. 285, p. 120482, 2023. doi: 10.1016/j.neuroimage.2023.120482.
- [36] D. J. Gale, R. Vos de Wael, O. Benkarim, and B. Bernhardt, *Surfplot: Publication-ready brain surface figures*, version v0.1.0, Oct. 2021. doi: 10.5281/zenodo.5567926. [Online]. Available: <https://doi.org/10.5281/zenodo.5567926>.
- [37] R. Vos de Wael, O. Benkarim, C. Paquola, *et al.*, “Brainspace: A toolbox for the analysis of macroscale gradients in neuroimaging and connectomics datasets,” *Communications Biology*, vol. 3, p. 103, Feb. 2020. doi: 10.1038/s42003-020-0794-7. [Online]. Available: <https://doi.org/10.1038/s42003-020-0794-7>.
- [38] E. Maris and R. Oostenveld, “Nonparametric statistical testing of eeg- and meg-data,” *Journal of Neuroscience Methods*, vol. 164, no. 1, pp. 177–190, 2007. doi: 10.1016/j.jneumeth.2007.03.024.

## A.0 Appendix

### A.1 Literature Values from Havlicek et al. and Novelli et al.

**Table 4**

Recommended parameter values for P-DCM and their plausible ranges (in brackets), with comparative values from Novelli et al.

Parameter	Name	P-DCM (Range)	Novelli et al.
<i>Intrinsic neuronal connectivity</i>			
$\sigma$ (Hz)	Excitatory self-connection	0.5 (0.1–1.5)	–
$\mu$ (Hz)	Inhibitory–excitatory connection	0.4 (0–1.5)	–
$\lambda$ (Hz)	Inhibitory gain factor	0.2 (0–0.3)	–
<i>Neurovascular coupling</i>			
$\varphi$ (Hz)	Decay of vasoactive signal	0.6	0.6
$\phi$ (Hz)	Gain of vasoactive signal	1.5	1.5
$\chi$ (Hz)	Decay of blood inflow signal	0.6	0.6
<i>Hemodynamic model</i>			
$t_{MTT}$ (sec)	Mean transit time	2 (1–5)	2
$\tau$ (sec)	Viscoelastic time	4 (0–30)	4
$\alpha$	Grubb's exponent	0.32	0.32
$E_0$	Oxygen extraction fraction at rest	0.4	0.4
<i>Physical BOLD signal model</i>			
$V_0$ (%)	Venous blood volume fraction	4	4

*Note.* For P-DCM and spDCM parameters, Optuna initial search ranges were defined as  $\pm 0.5$  around the literature-recommended value, or within the specified min–max range if provided.

## A.2 ROI Indices and Corresponding Functional Network

**Table 5**

Mapping of ROI index ranges to corresponding functional brain networks based on the 100-region Schaefer parcellation.

ROI Index Range	Functional Network / Region
0–8	Left Hemisphere Visual Network (LH VIS)
50–57	Right Hemisphere Visual Network (RH VIS)
9–14	Left Hemisphere Somatomotor Network (LH SM)
58–65	Right Hemisphere Somatomotor Network (RH SM)
15–22	Left Hemisphere Dorsal Attention Network (LH DA)
66–72	Right Hemisphere Dorsal Attention Network (RH DA)
23–29	Left Hemisphere Salience / Ventral Attention Network (LH SAL/VA)
73–77	Right Hemisphere Salience / Ventral Attention Network (RH SAL/VA)
30–32	Left Hemisphere Limbic Network (LH Limbic)
78–79	Right Hemisphere Limbic Network (RH Limbic)
33–36	Left Hemisphere Control / Frontoparietal Network (LH FPN)
80–88	Right Hemisphere Control / Frontoparietal Network (RH FPN)
37–49	Left Hemisphere Default Mode Network (LH DMN)
89–99	Right Hemisphere Default Mode Network (RH DMN)

### A.3 P-DCM vs spDCM Correlation

**Table 6**

Correlation analysis of parameter estimates from P-DCM and spDCM models under PLCB condition.

Parameter	Pearson r	p-value
$E_0$	0.0238	0.4320
$\alpha$	-0.0076	0.8010
$\alpha_e$	0.0493	0.1032
$\alpha_v$	0.0328	0.2783
$\beta_e$	0.0082	0.7859
$\beta_v$	-0.0478	0.1140
$\chi$	-0.0139	0.6465
$\tau$	-0.0506	0.0945
$\phi$	-0.0506	0.4887
$\tau_1$	0.0376	0.2134
$\varphi$	-0.0229	0.4497

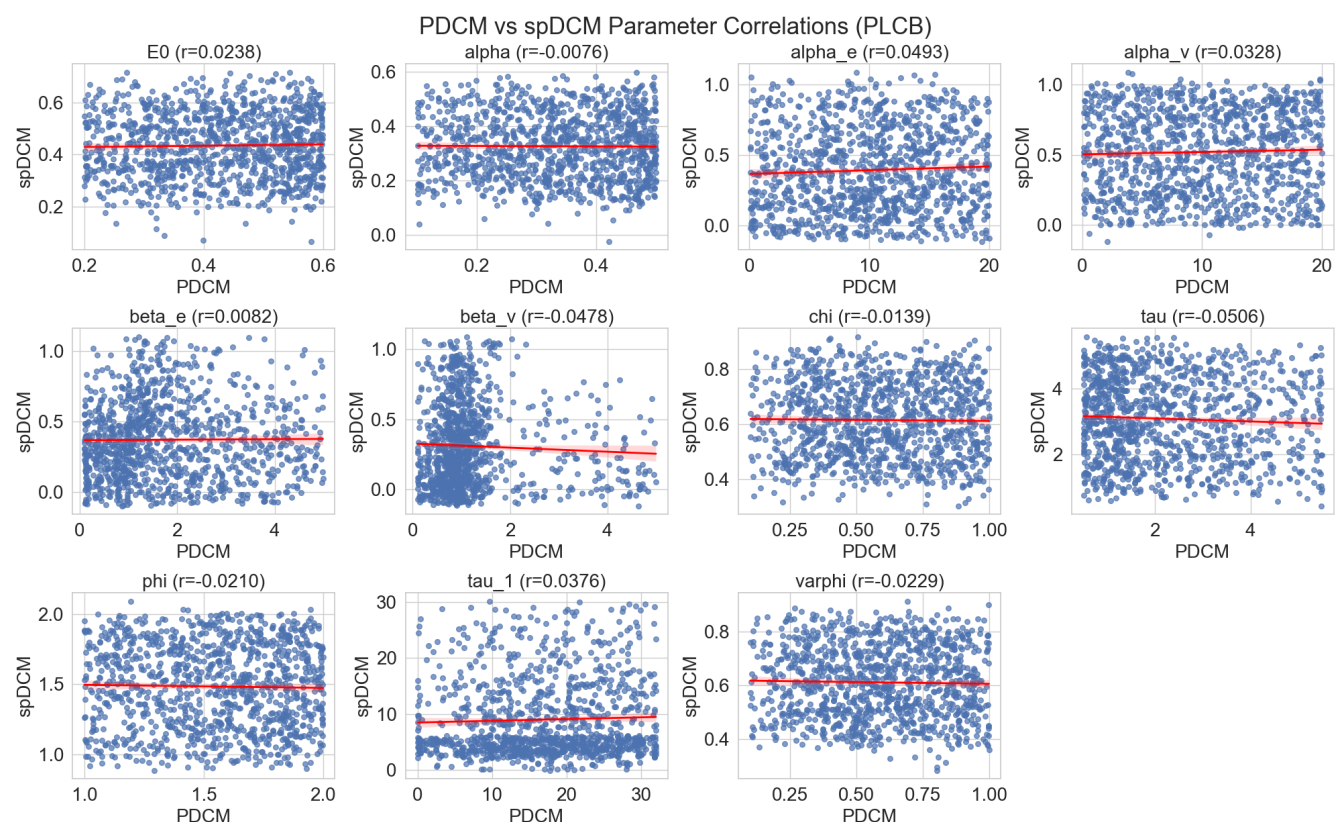


**Figure 12.** Scatterplots of parameter estimates from P-DCM vs. spDCM under the PLCB condition. Each subplot shows the relationship for one parameter, with Pearson correlation coefficients ( $r$ ) indicated.

#### A.4 Cortical Surface Projections of LSD vs. PLCB Parameter Differences (Paired *t*-tests)

To complement the analyses in the main text, this section presents cortical surface maps for a few more physiological parameters ( $\varphi, \chi, \alpha, \tau_1$ ) estimated by P-DCM and spDCM. Comparisons are made between LSD and PLCB conditions ( $-\log_{10}(p)$ , *t*-statistic and Cohen's *d* values)

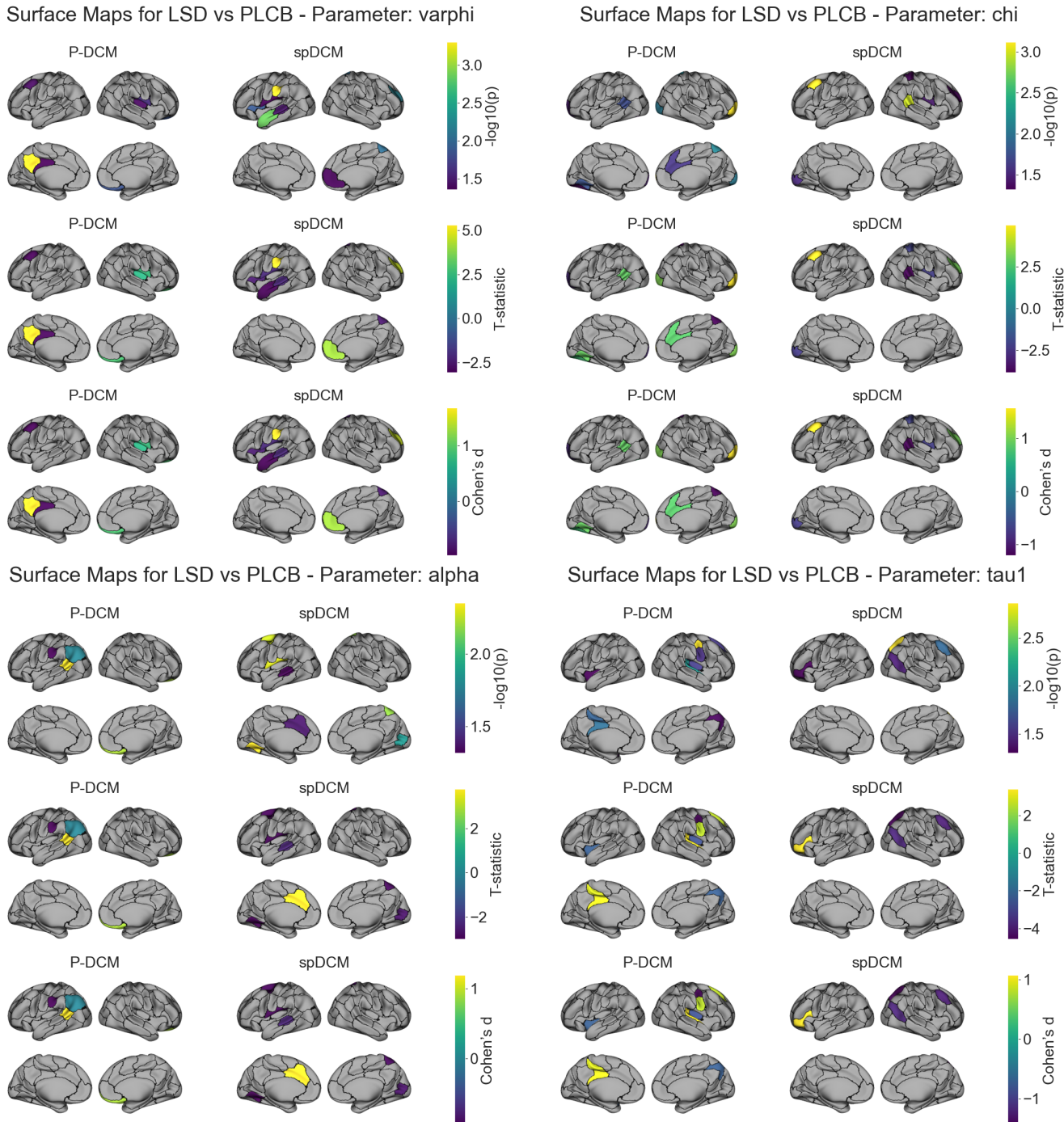


**Figure 13.** Cortical surface projections comparing LSD vs PLCB for parameters ( $\varphi, \chi, \alpha, \tau_1$ ). Left: P-DCM. Right: spDCM. Rows show  $-\log_{10}(p)$ , *t*-statistics, and Cohen's *d*. Bright colors indicate regions exceeding the uncorrected threshold of  $p < 0.05$  ( $-\log_{10}(p) > 1.3$ ).

## A.5 Network-Level Statistical Maps for Parameter Estimates

### P-DCM Model Results

Parameter estimates were averaged within each of the functional networks and across all cortical regions with significant p-values per subject. Paired-sample t-tests (uncorrected) comparing LSD and PLCB conditions were conducted for each parameter. Results are visualised through hierarchical clustering of  $-\log_{10}(p)$  values, t-statistics, and Cohen's  $d$  effect sizes.

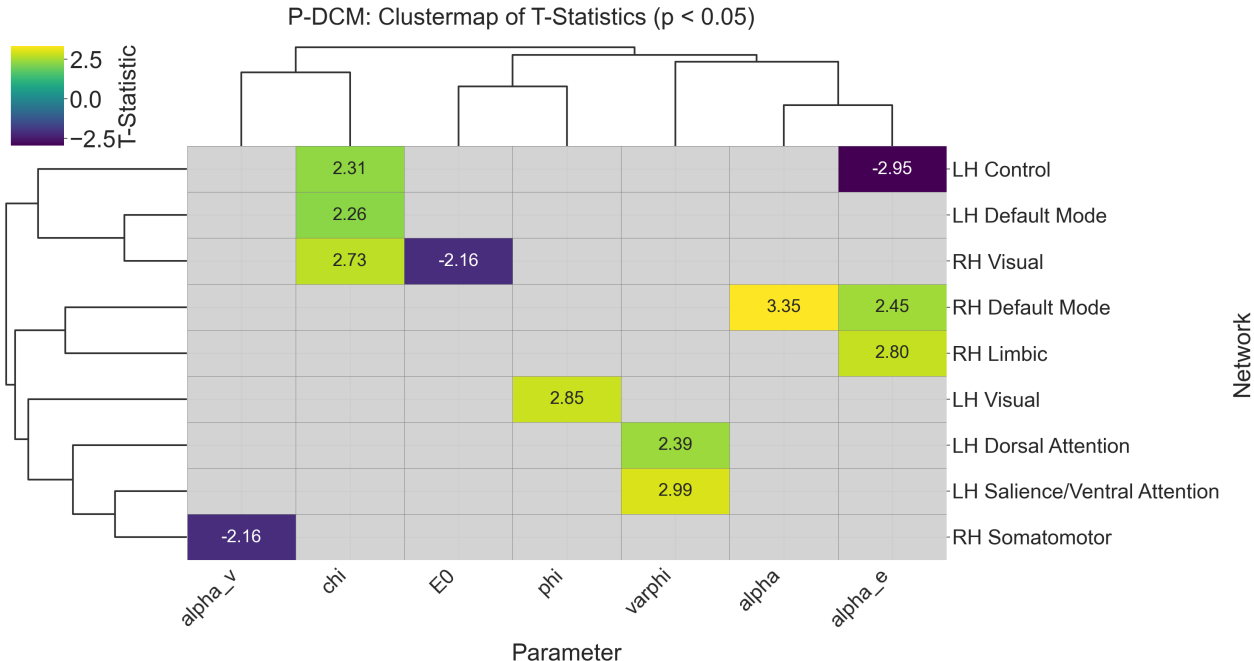


**Figure 14.** Clustermap of uncorrected paired  $t$ -test statistics (LSD vs. PLCB) for P-DCM parameter estimates across networks.

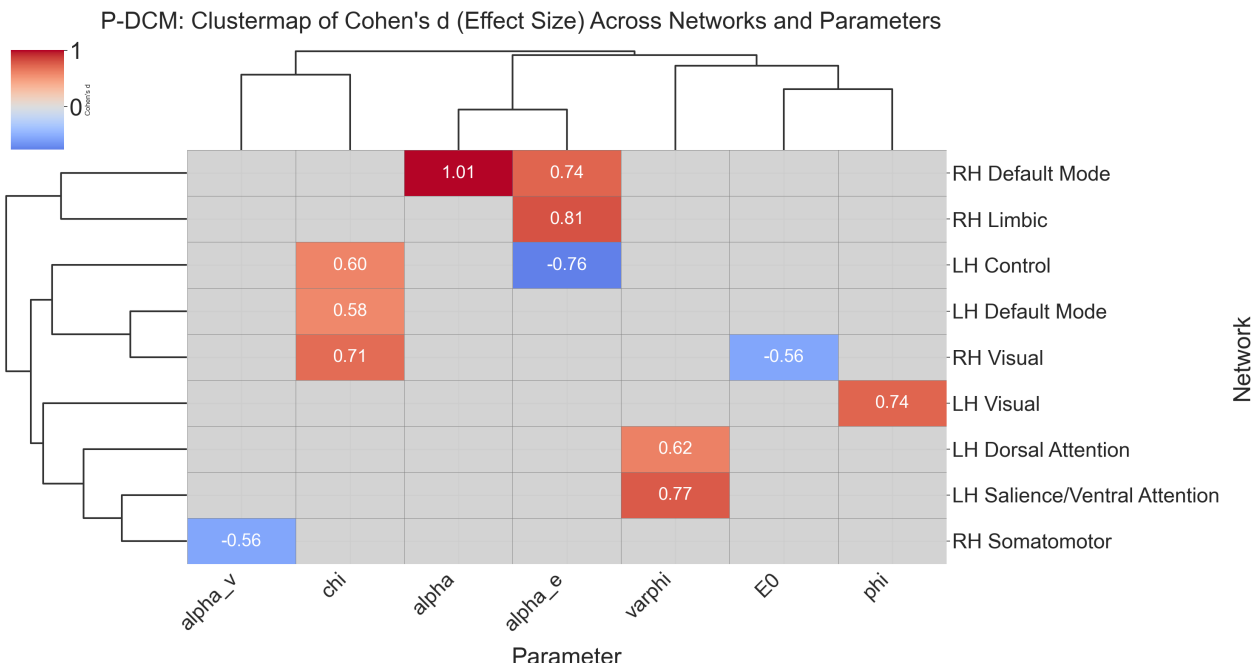


**Figure 15.** Clustermap of Cohen's  $d$  effect sizes from uncorrected paired  $t$ -tests (LSD vs. PLCB) for P-DCM parameter estimates.

## spDCM Model Results

Corresponding network-level statistics for the spDCM model are presented in Figures 16 and 17, showing uncorrected t-statistics and effect sizes.

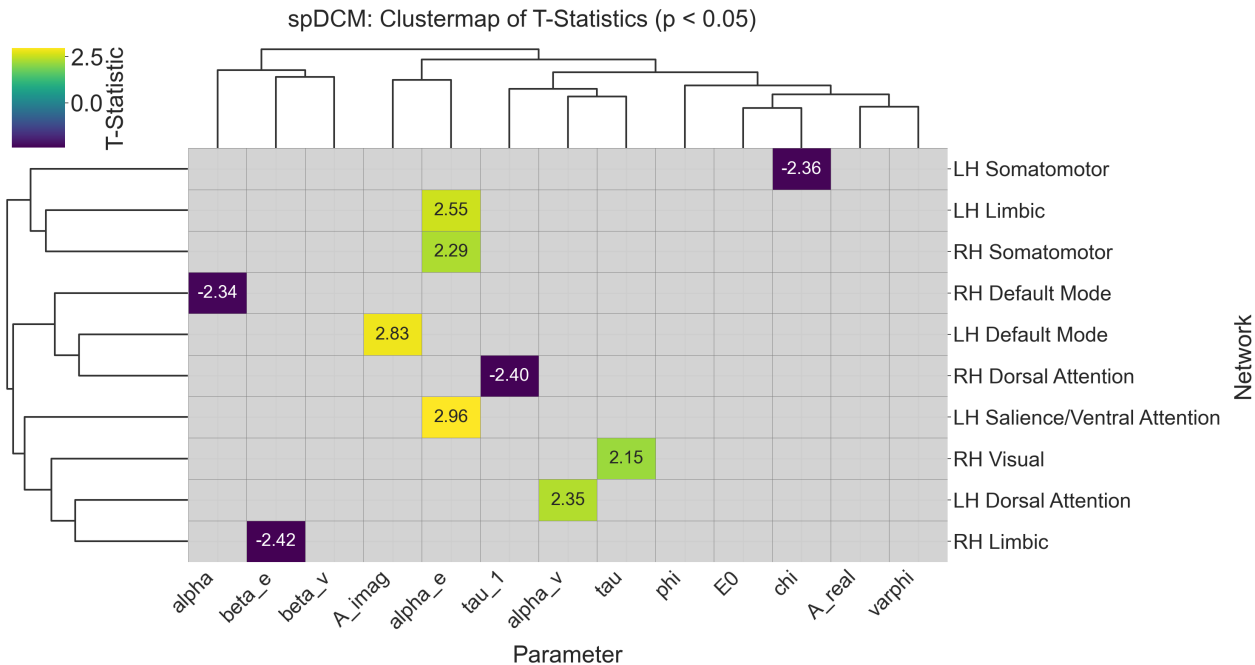


**Figure 16.** Clustermap of uncorrected paired  $t$ -test statistics (LSD vs. PLCB) for spDCM parameter estimates across networks.

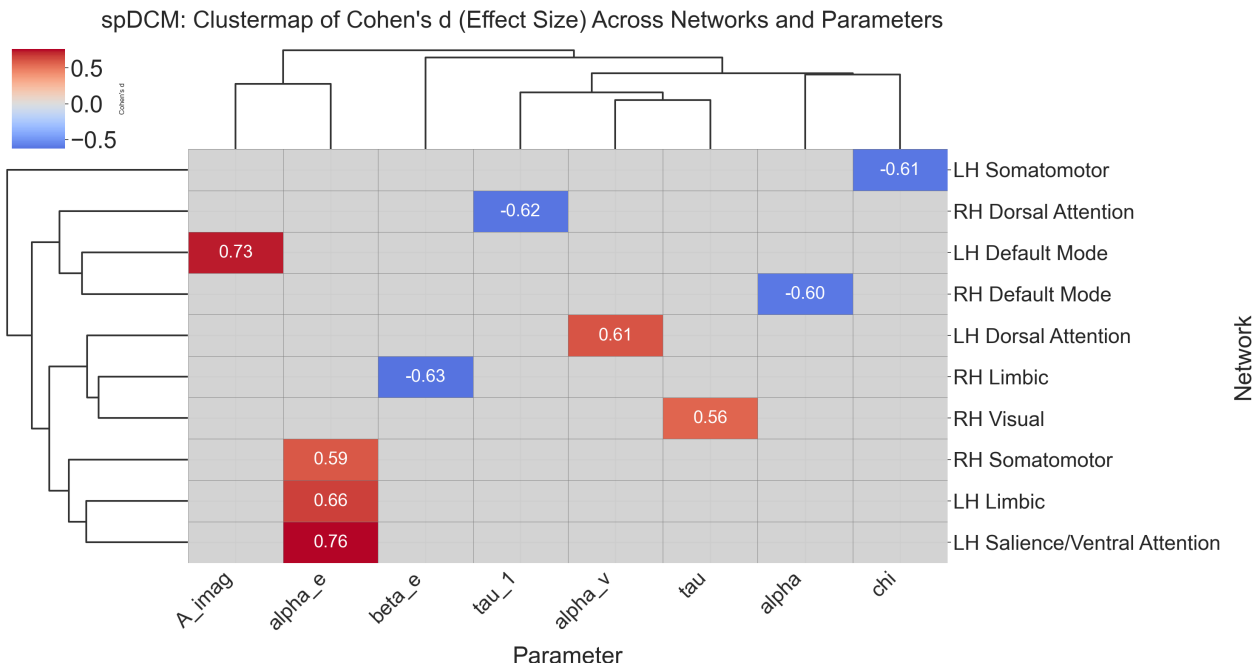


**Figure 17.** Clustermap of Cohen's  $d$  effect sizes from uncorrected paired  $t$ -tests (LSD vs. PLCB) for spDCM parameter estimates.